

Self-cleaned Photonic-enhanced Solar Cells with Nanostructured Parylene-C

*Pedro Centeno**, Miguel F. Alexandre, Manuel Chapa, Joana Pinto, Jonas Deuermeier, Tiago Mateus, Elvira Fortunato, Rodrigo Martins, Hugo Águas*, Manuel J. Mendes*

i3N/CENIMAT, Department of Materials Science, Faculty of Science and Technology, Universidade NOVA de Lisboa and CEMOP/UNINOVA, Campus de Caparica, 2829-516 Caparica, Portugal

*Corresponding authors: p.centeno@campus.fct.unl.pt, hma@fct.unl.pt, mj.mendes@fct.unl.pt

Abstract

Photonic front-coatings with self-cleaning properties are presented as means to enhance the efficiency and outdoor performance of thin-film solar cells, via optical enhancement while simultaneously minimizing soiling-related losses. This was achieved by structuring parylene-C transparent encapsulants using a low-cost and highly-scalable colloidal-lithography methodology. As a result, superhydrophobic surfaces with broadband light-trapping properties were developed. The optimized parylene coatings show remarkably high water contact angles of up to 165.6° and extremely low adhesion, allowing effective surface self-cleaning.

The controlled nano/micro-structuring of the surface features also generates strong anti-reflection and light scattering effects, corroborated by numeric electromagnetic modeling, which lead to pronounced photocurrent enhancement along the UV-Visible-Infrared range. The impact of these photonic-structured encapsulants is demonstrated on nanocrystalline silicon solar cells, that show short-circuit current density gains of up to 23.6%, relative to planar reference cells. Furthermore, the improvement of the devices' angular response enables an enhancement of up to 35.2% in the average daily power generation.

Keywords: Photovoltaics, Light management, Self-cleaning, Superhydrophobicity, Colloidal-lithography

1 Introduction

Accumulation of dust, snow or other particles on solar panels hinders light capture and promotes faster degradation (e.g. via hot-spot formation),^[1] leading to severe unpredictability in the devices' response and to efficiency losses (e.g. reaching 11% in 3 days and 65% after 6 months in certain power plants).^[2-5] This represents a significant cost in large-scale photovoltaic (PV) installations, as not only is the power generated by the dusty panels affected, but periodic cleaning is also mandatory. Several self-cleaning methods have been introduced to solve this problem.^[2] As it stands, the preferred approach uses mechanical techniques, such as brushing, air-blowing, water-blowing and ultrasonic vibration, which are expensive, require manual labor and have an inefficient, excessive use of water.^[2] Electrodynamic screens^[6] that repel dust particles by applying an electric-field on the panels' surface have also been investigated, however, despite improving the resources' usage efficiency, they require high voltages (900 V) and additional circuitry, increasing complexity and costs. Other promising approaches involve the use of super-hydrophobic/philic coatings,^[7-10] through the extreme tuning of surface wettability. Super-hydrophilicity can be particularly interesting for anti-fogging technologies, while superhydrophobicity can be preferential for anti-soiling functionalities needed in PV. Inspired by plant leaves (e.g. *Nelumbo nucifera*, commonly known as Lotus flower) with self-cleaning capability^[11], superhydrophobic coatings possess conspicuously low surface energy,^[12] allowing water droplets to easily roll down the coatings' surface, carrying away any existing dust particles, thus producing a biomimetic self-cleaning effect.^[8] Moreover, as explored here, the wavelength-sized nano/micro-structures required for the geometric-based superhydrophobic behavior are well in range with those studied for light-trapping purposes, thence permitting improvements in the solar cells' optical performance.^[13-16]

The increasing interest in thin-film PV has promoted the development of lighter, flexible cells, effectively broadening its applicability, while reducing raw material usage and production costs.^[16,17] Nonetheless, the limitations imposed by the thin absorber regions compromise photocurrent generation due to reduced sunlight absorption. To address this issue, several light-trapping (LT) mechanisms have been proposed,^[13-19] revealing broadband optical enhancements that compensate for the lower thickness. First, anti-reflection (AR) coatings are mainly used to improve absorption in the UV-visible range, using gradual refractive-index matching and/or geometric index matching.^[14,15,20-22]

Secondly, scattering elements (front and/or rear placed) enable higher near-infrared absorption through optical path length amplification within the thin absorbers.^[20,22,23]

Here, we present a photonic superhydrophobic front-coating that produces a self-cleaning effect and also enhances the optoelectronic performance of thin-film solar cells. Parylene-C [poly(chloro-p-xylylene), henceforth parylene] was the preferred coating material, since it is an extremely stable polymer with excellent barrier properties for encapsulation^[24–29] and low surface energy. Furthermore, it benefits from optical transparency^[30] and adequate refractive-index for AR purposes, conjoined with outstanding flexibility and mechanical strength.^[8] Moreover, parylene is deposited via chemical vapor deposition, that allows for the deposition of extremely conformable coatings at room temperature, thus enabling its use with non-flat temperature-sensitive materials.^[24,30,31]

The parylene's hydrophobicity can be controlled by adjusting the surface corrugations (i.e. roughness, patterned features) and surface chemical composition.^[8,12,32–34] Although several surface treatment methods can be employed, most of them present issues that can result in low surface uniformity or polymer degradation.^[31] In this work, a low-cost, scalable plasma-based soft-lithography technique – colloidal-lithography (CL)^[17,20] – was developed to produce a patterned honeycomb array of tapered-cone microstructures that enable superhydrophobicity while simultaneously allowing geometric-based AR and scattering effects.

The overall influence of the corrugations on water contact angle (CA) is described by two well-known models – Wenzel^[35] and Cassie-Baxter,^[36] depicted in Figure 1. The Wenzel model postulates that there is total water impregnation within the rough surface (i.e. only a solid-liquid interface occurs at the base of the droplet) and that introducing surface roughness always intensifies the original wetting properties. Oppositely, the Cassie-Baxter model assumes that there is no water impregnation, so air pockets are created in the cavities between the rough solid surface and the liquid. A given surface in this state exhibits lower adhesive behavior than in the Wenzel state^[12] and a larger CA than the corresponding flat surface,^[36] allowing an easier droplet roll-off, which enables the desired self-cleaning capability. Nonetheless, several studies^[37–40] have reported the existence of a transitional wetting state, between the Wenzel and Cassie-Baxter states, where the water droplet partially impregnates the surface's texture (see Figure 1).

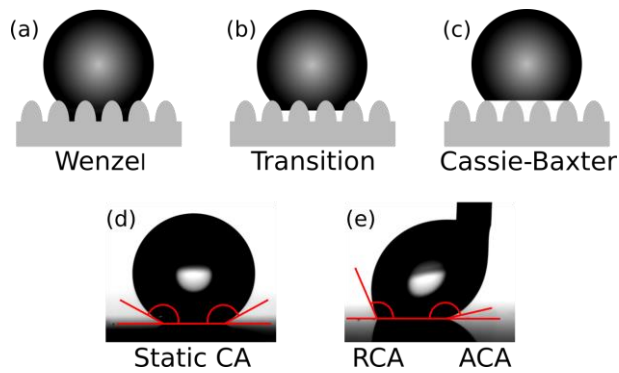


Figure 1 – The top sketches illustrate surface wetting in: (a) the Wenzel state, (b) transition state and (c) Cassie-Baxter (CB) state. The bottom photos of water droplets on a hydrophobic surface show the: (d) static contact angle (CA) and (e) dynamic CAs (receding, RCA, and advancing, ACA).

Besides surface roughness, further improvements can be achieved by changing the surface chemical composition. The introduction of oxygen functional groups, via O_2 reactive-ion etching (RIE), on a surface enhances its hydrophilicity, whereas fluorinated functional groups, via SF_6 RIE, intensify the hydrophobicity.^[8,12,34,41] Interestingly, the application of O_2 RIE activates the surface, due to the formation of new oxygen-related chemical bonds, which then facilitates the reaction with SF_6 plasma, switching the wettability.^[8]

2 Results and Discussion

2.1 Surface Modification via Plasma-based Colloidal-Lithography

The patterning approach explored here, via a plasma-based colloidal-lithography (CL) process^[17,20] (Figure 2), allows the tailoring of surface roughness and chemistry simultaneously. The method comprises the deposition of a closed-packed honeycomb monolayer of self-assembled polystyrene (PS) colloidal microspheres which serves as mask for the subsequent surface patterning through RIE. This procedure enables the precise micro-patterning of parylene with tapered micro-structured features, having the same periodicity as the PS monolayer used as mask. In this study, two RIE procedures have been evaluated, using either solely SF_6 or O_2 followed by a short (1 min) SF_6 post-RIE (henceforth O_2+SF_6 RIE), and the main differences regarding etching rate, microstructure's geometry (consequently LT properties) and influence on surface wettability were analyzed.

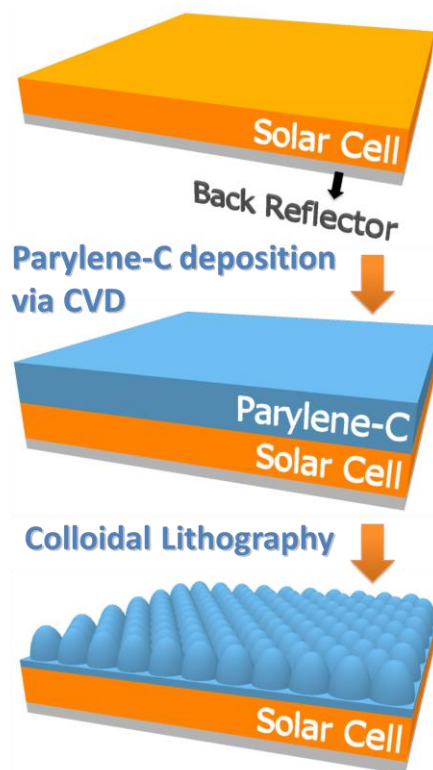


Figure 2 – Depiction of the patterning of the photonic-structured parylene coating, on the transparent front contact of the solar cells, via chemical vapor deposition (CVD) followed by colloidal-lithography (CL). The advantageous wettability and light-trapping properties provided by the nanostructured parylene are evaluated by comparison with the uncoated (top image) and flat parylene coated (middle image) cells.

2.1.1 Surface Topography

Using RIE in CL patterning is a particularly attractive approach to alter surface topography due to both low processing temperature (ambient) and scalability, thus being highly advantageous for industrial implementation. Moreover, by adjusting the RIE conditions, the selective etching of materials and the etching directionality/isotropy can be tuned, which is paramount for the fabrication of high aspect-ratio structures.^[17] Figure 3a,b show SEM images of the structures obtained from CL using SF₆ and O₂+SF₆ RIE. Figure S1 in Supporting Information (SI) presents additional SEM images for different RIE times. Initially, the selectivity and directionality of the RIE process leads to the formation of cylindrical structures beneath the masking PS microspheres. The microspheres also suffer etching with exposure to plasma, thus reducing their diameter and progressively uncovering the underneath structures. This subsequently leads to the lateral etching of the microstructures, ultimately forming the tapered cone-like structures shown in Figure 3.

Both RIE procedures resulted in honeycomb arrays of tapered structures having a center-to-center distance equal to the initial diameter (1.6 μm) of the PS colloids. The influence of RIE on the microstructures' height is plotted in Figure 4a,b. The SEM analysis revealed that the final microstructures presented an average height of 1.59 and 1.67 μm and average base diameter of 1.08 and 1.19 μm , respectively with 80 min SF_6 and 10 min O_2+SF_6 RIE. However, the application of O_2+SF_6 RIE originated an additional random nano-roughness texture.^[8,24,29]

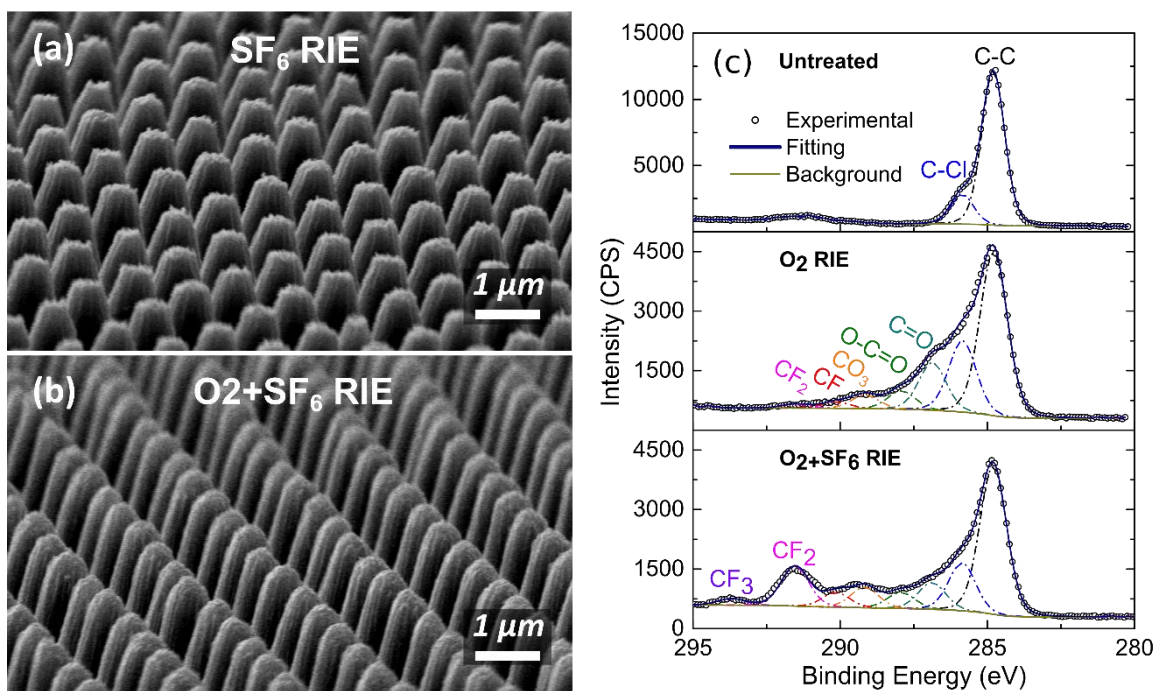


Figure 3 – SEM images of microstructured parylene surfaces after CL patterning with (a) 80 minutes SF_6 RIE and (b) 10 minutes O_2+SF_6 RIE. (c) XPS experimental spectra and corresponding fitted carbon 1s ($\text{C}1\text{s}$) spectra of untreated (top), 9 minutes O_2 RIE (middle) and 9 minutes O_2 followed by 1 minute SF_6 RIE (bottom) parylene surfaces.

2.1.2 Surface Chemistry Analysis

To understand the chemistry-related changes in wettability, we analyzed parylene samples with different treatments, representative of each O_2+SF_6 RIE stage, employing x-ray photoelectron spectroscopy (XPS). For this characterization, the RIE process was performed directly on the parylene, without the PS microspheres mask, to solely analyze the chemical effects produced by RIE. Figure 3c shows the carbon 1s ($\text{C}1\text{s}$) spectra and corresponding deconvoluted fitting of three parylene surfaces. Comparing with the untreated parylene, which mostly revealed the existence of carbon and chlorine

(C-C and C-Cl bonds at 284.8 and 285.9 eV, respectively), the O₂-treated sample predictably led to a substantial increase in oxygen atomic concentration (C=O at 286.9 eV, O-C=O at 287.9 eV and CO₃ at 291.5 eV^[42]). Here, the oxygen functional groups are responsible for the increase in surface free energy, which subsequently enhances the hydrophilicity. Two low-intensity peaks were also identified at 289.2 (CF) and 290.1 eV (CF₂) which may be related to negligible fluorine contaminations in the RIE chamber.^[8,41,42] The O₂+SF₆ RIE sample displayed a significant increase in fluorine atomic concentration (much stronger CF and CF₂ peaks, and a new CF₃ peak appeared at 293.7 eV^[8,41,42]) and a decrease in oxygen concentration, suggesting a partial substitution of oxygen by fluorine functional groups,^[41] mainly CF₂.

The O₂ plasma provided the activation of the parylene surface, subsequently allowing the reaction of fluorine with oxygen, when exposed to SF₆ plasma.^[8,41] The chemical inertness of the fluorinated groups, therefore, contributes to the lowering of the surface energy, which in turn improves the hydrophobicity.^[8,12]

2.2 Contact Angle (CA) Measurements

To enable an effective self-cleaning (water-repelling) effect on PV modules the surface must not only exhibit superhydrophobicity (i.e. static CA above 150°), but also allow an easy water roll-off which is assessed by the hysteresis of the dynamic CA (Figure 1).^[8,12] As such, the wetting behavior of both microstructured parylene coatings shown in Figure 3 is evaluated by the static, advancing (ACA) and receding (RCA) water contact angles presented in Figure 4c,d (see also Figure S2 in SI).

The untreated parylene (i.e. without RIE application) exhibited a low static CA (95.8°). After applying O₂ pre-RIE the parylene surface became superhydrophilic^[32] (CA<10°), causing water droplets to completely wet the parylene which consequently precluded the CA measurement.^[41] This is due to the introduction of oxygen polar functional groups,^[43–45] as indicated by the XPS results (Figure 3c). The application of 1 min of SF₆ post-RIE switched the surface wettability from hydrophilic to hydrophobic, regardless of the previous O₂ RIE time. As expected, it was observed that increasing RIE time results in improved static CA, exceeding 150° with 8 min of O₂+SF₆ RIE and 70 min of SF₆-only RIE.

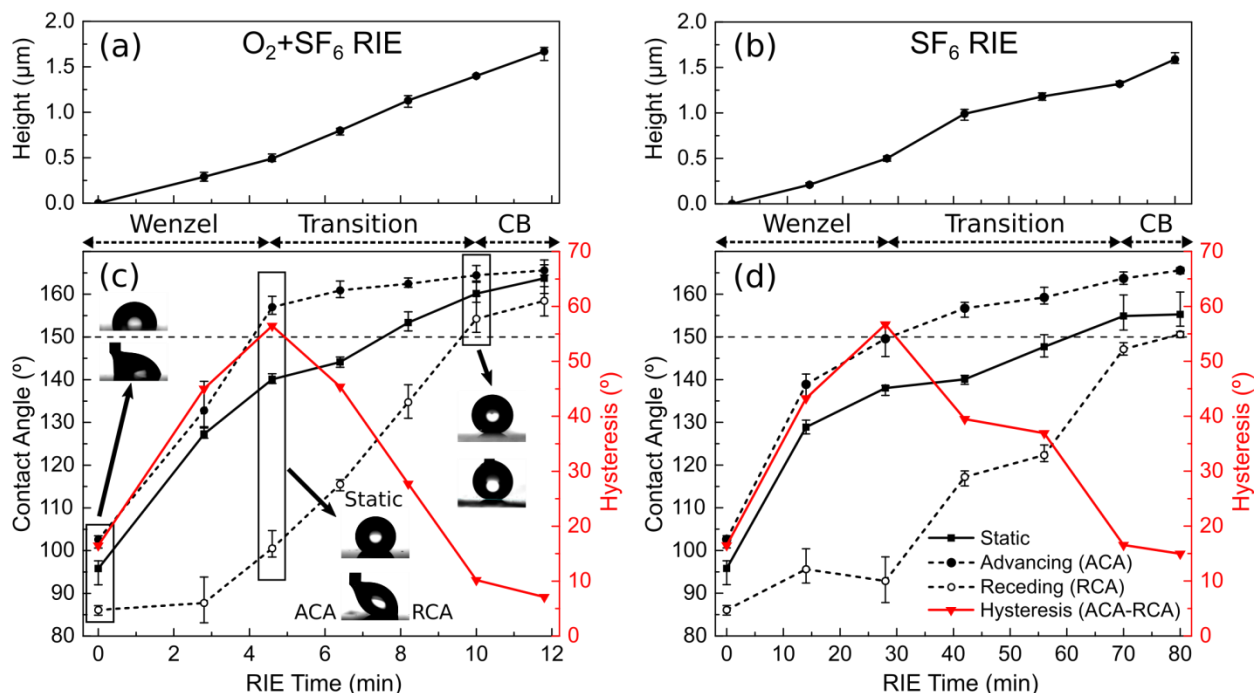


Figure 4 – Static and dynamic (advancing, ACA, and receding, RCA) water contact angles (black curves), together with the hysteresis (ACA-RCA – red curves), for O_2+SF_6 RIE (c) or SF_6 RIE (d) structured parylene surfaces, as a function of RIE time. These wettability properties are compared with the height of the etched microstructures, represented respectively in the top plots (a) and (b), which can be visualized in the SEMs of Figure 3 and S1. The error bars show the value span of each measure. The insets in (c) show representative images of water droplets on the structured parylene coating, illustrating the static (top photos) or dynamic (bottom photos) shape of the droplets on the untreated flat surface (left), in the Wenzel state (middle) and in the Cassier-Baxter (CB) state (right). Both O_2+SF_6 and SF_6 treatments attained similar values for the different contact angles, albeit at quite distinct RIE times. Therefore, the droplet images are only shown in (c) and not in (d), since they are similar for both cases. Figure S2 in SI shows more detailed droplet profiles on surfaces with different O_2+SF_6 RIE times.

The dynamic ACA and RCA allow a deeper insight on the water droplet state, and the lower their hysteresis ($Hys=ACA-RCA$) the easier is the water roll-off. These measurements indicate the presence of three wettability states indicated in Figure 4. Looking first at the O_2+SF_6 RIE treated samples (Figure 4c and S2), the initial state comprises not only the aforementioned untreated flat sample (RIE time=0), whose wettability is governed solely by its chemical properties, thus displaying relatively low hysteresis (16.5°), but also the samples with $RIE < 5$ min, that present low aspect-ratio microstructures (< 500 nm height, see Figure S1). Despite showing increased static CA (140°), the hysteresis suffered a striking increase (up to 57°), due to total water impregnation between the patterned microstructures, which is

characteristic of the Wenzel state. This translates in a pronounced pinning effect (i.e. water droplets “stick” to the surface), which is not beneficial for self-cleaning. In the second state (RIE from 5 to 10 min), we registered a smooth CA hysteresis decrease that is related to the increasing microstructures’ height (from 500 nm to 1.4 μm). In accordance with other studies,^[46–49] this evidences a transition state between Wenzel and Cassie-Baxter states where partial water impregnation occurs. The last state (RIE>10 min) is characterized by the Cassie-Baxter state, where the CA hysteresis saturated with values below 10°, showing rather low adhesive behavior and extremely high static CA (reaching 165.6° with 12 min O₂+SF₆ RIE). This is due to the increase of the microstructures’ height (>1.4 μm), allowing an easy droplet roll-off and, subsequently, the desired self-cleaning functionality.

Concerning the SF₆-only treated surface (Figure 4d), its wettability behavior is very similar to the previous one, differing only in the much higher RIE exposure time. The desired Cassier-Baxter state was obtained only after 70 min RIE, however with a lower maximum static CA (155.3° with 80 min) and higher hysteresis, as compared with the O₂+SF₆ RIE of Figure 4c.

2.3 Photonic-enhanced Solar Cells

The optical properties of the microstructured parylene coatings were preliminarily assessed on transparent substrates (glass, see section S3 of SI), but their light-trapping (LT) effects can only be evaluated after application on the PV devices. For that, the super-hydrophobic 10 min O₂+SF₆ RIE (henceforward O₂+SF₆ RIE) and 80 min SF₆ RIE (henceforward SF₆ RIE) coatings were integrated on hydrogenated nanocrystalline silicon (nc-Si:H) solar cells with n-i-p (substrate-type) configuration (see Experimental Section), having the layer structure: 120+60 nm Al+AZO (rear contact)/30+1250+12 nm n+i+p nc-Si:H (junction)/230 nm IZO (transparent front contact).

2.3.1 Spectral Response

The application of the water-repealing photonic coatings on the nc-Si:H cells significantly improved their optical absorption and external quantum efficiency (EQE) spectra, as shown in Figure 5. At short wavelengths below 400 nm, the absorption is much higher than the EQE due to the parasitic absorption at the cell front occurring in the parylene^[50] and in the transparent conductive contact (TCO) made of indium zinc oxide (IZO).^[51] This performance loss in the UV is easily atoned by the LT gains at longer wavelengths.

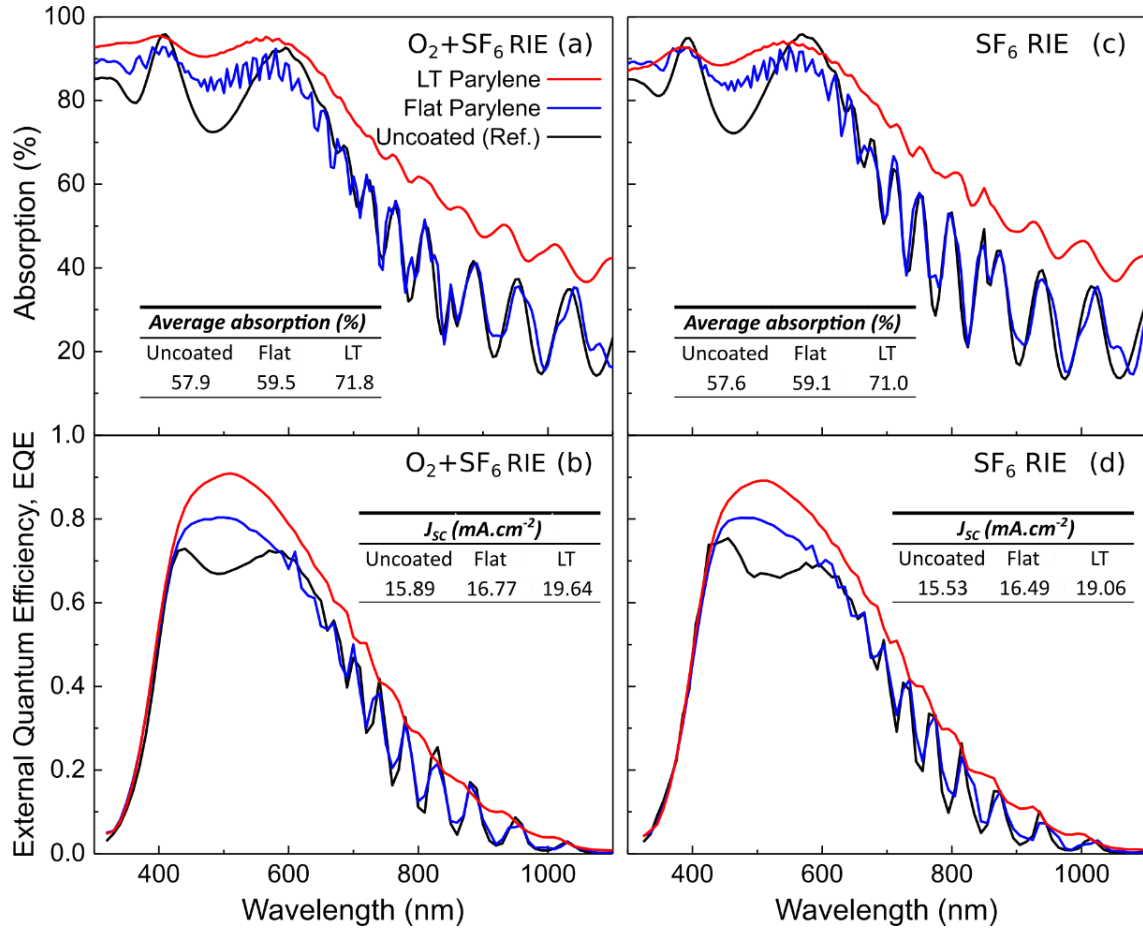


Figure 5 – Absorption (a,c) and external quantum efficiency, EQE (b,d), spectra of two representative nc-Si:H solar cells measured before (uncoated reference, in black) and after (flat parylene, in blue) the application of the parylene top layer, as well as after its colloidal-lithography patterning (LT parylene, in red), to enable LT and self-cleaning functionality, using O_2+SF_6 RIE (a,b) and SF_6 -only RIE (c,d). The inset tables show the average absorption (a,c) and J_{sc} (b,d) calculated by integration of the full measured spectra.

In the visible range (400-600 nm), the simple addition of the flat (unstructured) parylene layer on top of the device decreases the light exiting the cells, since such layer provides an anti-reflection (AR) effect. Namely, the refractive-index matching provided by the intermediate index ($n=1.6$) of parylene, between that of air and the front IZO ($n=1.9$), provides an increase of the average total absorption, resulting in 9.6% EQE improvement in this spectral region relative to the reference cell without parylene. Nevertheless, with the micro-structured coating there is a much stronger suppression of reflection, as a consequence of the more efficient geometric index matching provided by the patterned

tapered-cone shape of the microstructures, resulting in an EQE increase of up to 21.8% in the same wavelength range.

In the red-near-IR range (>600 nm wavelengths) further improvements were obtained from the scattering effect provided by the photonic-structured parylene coating. Scattering redirects the light rays away from the illumination direction, therefore disrupting the light-wave interference occurring in the flat cells which causes the sharp peaks, observed in Figure 5, at longer wavelengths. Besides attenuating the interference peaks, scattering enhances the optical path length of the rays inside the absorber,^[15,52] thereby providing improved absorption (yielding up to 31.0% EQE enhancement in this range). However, the absorption is higher than the EQE, but now mainly due to parasitic absorption in the rear contact.

Overall, the EQE results show that the sole addition of the flat parylene layer enabled a short-circuit current density (J_{SC}) enhancement up to 6.2% relative to the uncoated solar cell. Nevertheless, with the microstructured parylene, this photocurrent gain rises to 22.8% and 23.6% using SF₆ RIE and O₂+SF₆ RIE, respectively, due to the broadband LT effects (AR+Scattering).

2.3.2 Angular Response

The cells' angular response was analyzed to evaluate the photonic coatings for application in non-tracking PV installations and/or in flexible thin-film PV modules mounted on curved/bendable platforms.^[53] Ideally, an omnidirectional response is desired to enable maximum power output regardless of the device's curvature or light incidence angle (LIA).

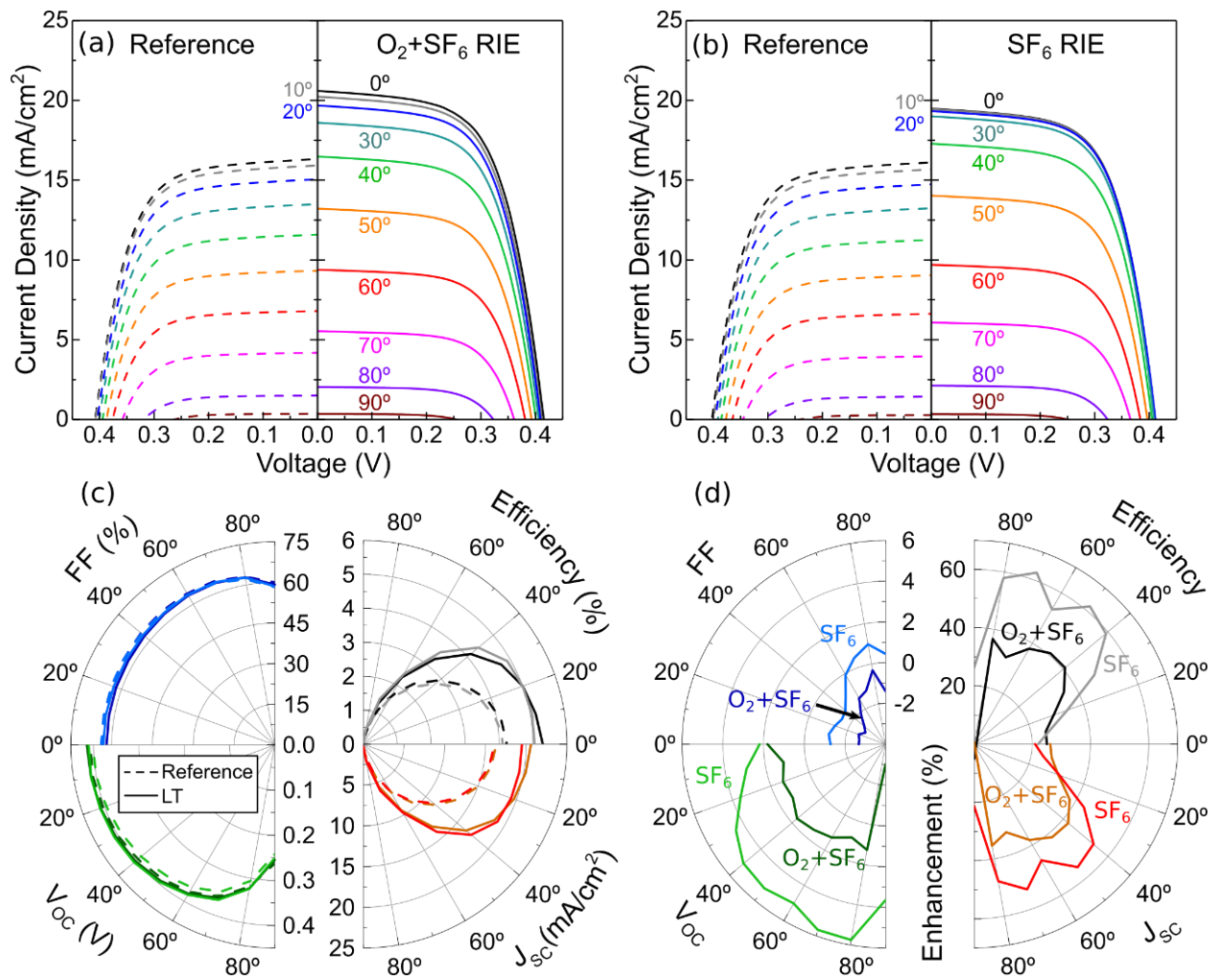


Figure 6 – (a,b) 1-Sun J-V curves of the solar cells before (uncoated reference, left curves) and after (right curves) coating with the photonic-structured parylene, for illumination angles varying from 0° (illumination normal to cell’s surface) to 90° (parallel to surface), corresponding to the samples etched with (a) O₂+SF₆ RIE and (b) SF₆ RIE. (c) Polar plots representing the angular response of the cells with O₂+SF₆ and SF₆-only RIE parylene coating [labels indicated in (d)] in terms of efficiency, J_{sc}, V_{oc} and FF. The solid lines correspond to the cells with the photonic-structured parylene and the dashed ones to the respective references. (d) Polar plots with the relative enhancements of the quantities represented in c) with respect to the uncoated references.

Figure 6 shows the angular measurements of the nc-Si:H cells with two different LT coatings obtained from the 9 min O₂+SF₆ and 80 min SF₆-only RIE procedures during the CL processing. Figure 6a,b display the J-V curves with LIA ranging from 0° (illumination normal to cell’s surface) to 90°. The first aspect here reported is the pronounced J_{sc} enhancement, relative to the uncoated reference, not only for normal incidence (in accordance with the optical gains analyzed from Figure 5), but even higher for oblique illumination. As expected, the cells’ power output is negatively affected with increasing LIA due

to reflection losses. Nevertheless, the broadband AR effects, provided by the geometrical microstructuring and refractive-index of parylene, are able to highly reduce such losses.^[23] The polar plots of Figure 6c show the influence of LIA on the efficiency, J_{SC} , fill-factor (FF) and open-circuit voltage (V_{OC}) of the cells, with and without (reference) the LT parylene coating, while Figure 6d shows the corresponding relative enhancements. These results reveal that the enhancement in J_{SC} (and efficiency) increases with LIA up until 40°, and the gain is considerably higher for the SF₆-only etched coating with a peak enhancement at 50° LIA of 52% (and 61%), against 41% (and 40%) for the O₂+SF₆ etched coating. In addition, the SF₆-treated cells' efficiency remained practically constant when increasing LIA up to 30°, registering a decrease below 3% in relation to normal illumination, while the reference cell's efficiency decreased above 11%. Both V_{OC} and FF are slightly reduced with increasing LIA, however the application of the SF₆-treated parylene coating enabled a V_{OC} enhancement between 2.1% and 5.9% with increasing LIA, relative to the reference cell. Consequently, it is estimated that the SF₆-RIE and O₂+SF₆-RIE photonic-structured coatings allow substantial enhancements of 35.2% and 29.8%, respectively, of the average daily power supplied by the cells.

2.3.3 Electromagnetic Modelling

To gain a deeper understanding of the optical effects brought forth by the LT nanostructures, a finite-differences time-domain (FDTD) method^[54] was employed to assess the light-device interaction (Figure 7).^[20,53,55] This simulation technique uses the experimentally-measured broadband complex refractive-index ($N=n+ik$) of the device's materials, provided in Figure S4. Here, it should be noted that the absorption coefficient of the parylene coating was neglected (thus, its $k=0$), which is in general a good approximation when simulating thin optically non-absorbent layers.

The front LT features on the micro-structured parylene were modeled as an hexagonal array (honeycomb) of semi-spheroids with axis of revolution normal to the cell plane. The dimensions considered in the FDTD model were obtained from a 2-part process. First, the average dimensions of the photonic structures and composing cell layers were determined from SEM analysis. Subsequently, an optimization procedure, using the least squares method, was used to vary the device's dimensions around the experimentally measured value, thus ensuring the best fitting between experimental and theoretical measurements. The resulting values of the parameters considered in the simulations are presented in Table S1 in SI.

Figure 7a shows the simulated absorption of the solar cell structure coated with the microstructured parylene and the uncoated reference. Comparing the computed absorption with the corresponding measured spectra of Figure 5a, the first notable difference appears in the form of higher intensity interference peaks in the FDTD results.^[16,53] While the theoretical results consider fixed dimensions for the parylene microstructures and cell layers, the experimental spectra are influenced by small random variations in all the geometrical parameters of the fabricated cells across the measured area (2.5x2.5 cm). Such variations lead to less pronounced constructive interferences, as there are multiple lower intensity interferences from the parameter dispersion, thus leading to less intense and broader interference peaks.^[17,20] Apart from this inevitable difference, there is an almost perfect match regarding the peak positions and overall spectra behavior of the modeled and measured absorption profiles, thence validating the discussion of section 2.3.1 regarding the optical effects at play.

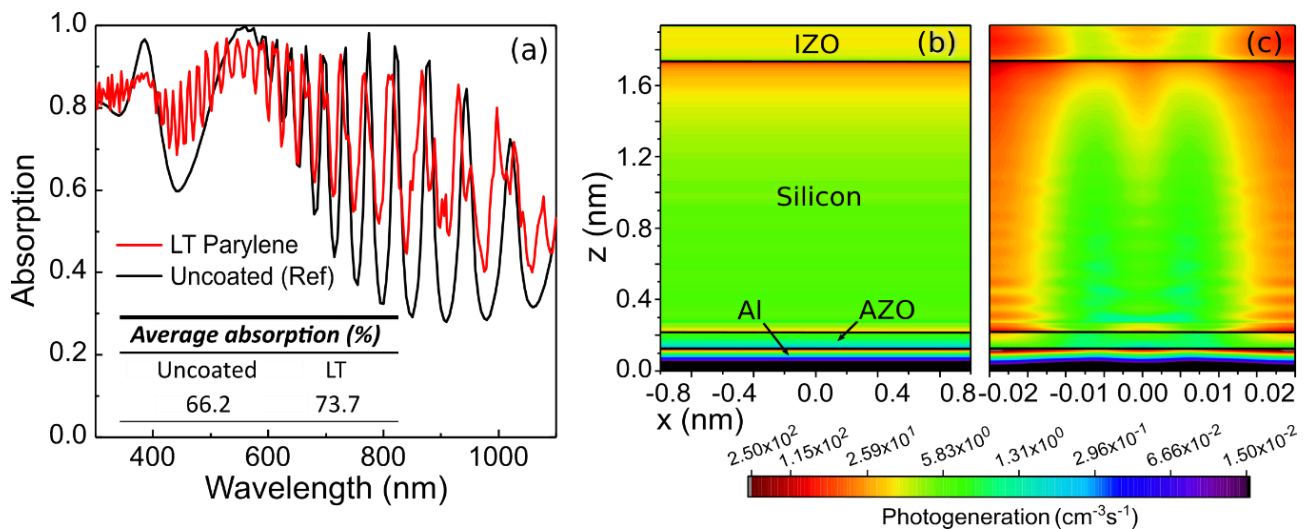


Figure 7 – (a) Absorption spectra obtained from the FDTD simulation of the reference solar cell, in black, and of the cell with the LT layer of parylene, in red. Corresponding photogeneration rate profiles for the reference cell (b) and the LT-enhanced cell having the structured parylene (not shown) on top of the front IZO contact (c).

Considering the transition from the reference to the LT-structured device, the experimental results are accurately mimicked by the simulation. First, above 600 nm wavelengths there is an overall absorption increase due to LT, conjoined with a lower magnitude of the interference peaks. It should be noted that, below 400 nm wavelengths the lower simulated absorption (relative to measured one) stems from the aforementioned approximation whereby the parylene’s absorption coefficient was kept at 0. However, since the parylene layer has a relatively large thickness (~6 μm), its total absorption

creates a small disparity between the experimental and simulated results in the UV range. Figure 7b,c show the photogeneration rate profiles for the reference and photonic-coated devices, respectively. Here, the absorption benefits brought forth by the LT structures atop the device are forthwith evidenced when compared with its non-structured counterpart. Moreover, it is conspicuous the significant increase in the device's absorption occurring in the bulk of the silicon layer. Electrically, bulk absorption is less prone to recombination losses when compared with surface absorption,^[55,56] thus delineating that these photonic structures are not simply limited to providing optical gains. Lastly, it should be noted that there is also an increase in the overall parasitic absorption, especially in IZO, however, the aforementioned increases far outweigh these losses and hence they can be vilipended.

3 Conclusions

In this work, we have shown a simple, low-temperature, low-cost and scalable colloidal-lithography method to engineer parylene-C coatings with encapsulating properties that endow effective light-trapping and water-repelling functionality when applied in thin-film solar cells. We explored the use of O₂ and SF₆-based RIE, with masking microspheres, for the controlled patterning of parylene with photonic structures.

The use of a 2-step O₂+SF₆ RIE process in the colloidal-lithography patterning allowed the formation of the desired microstructures with much shorter RIE duration (~8 times) than a 1-step SF₆-only RIE. While the O₂+SF₆ RIE was also advantageous regarding the resulting water-repelling surface properties, the SF₆-only RIE revealed superior light-trapping performance in the cells likely due to the more tapered (lower aspect-ratio) shape of the resulting features which increases their scattering cross-sections. For thin-film PV application, in view of its low-cost and high-throughput goals, the O₂+SF₆ would be the preferred approach, also supported by the fact that a core value pursued in our research is the strive for environmentally-friendly processes and solutions.

The experimental results established that surface roughness and chemistry modification from both approaches effectively provide superhydrophobicity with contact angle of up to 165.6° with extremely low adhesion, thus fulfilling the requirements for self-cleaning purposes. These micro-structured parylene coatings also enable outstanding anti-reflection and light scattering properties, as verified via FDTD simulation, that enhance the solar cells' photocurrent by up to 23.6% with normal incident light.

Furthermore, the improvement of the cells' angular response resulted in an estimated average daily power enhancement of up to 35.2% compared with the uncoated reference cells.

4 Experimental Methods

4.1.1 Solar cell fabrication

Substrates preparation. Glass slides with 10x10 cm were washed with a diluted MICRO-90 cleaning solution and rinsed with ultrapure water. After sonication in acetone and isopropanol for 15 minutes each, the substrates were rinsed in ultrapure water. Finally, they were dried under a nitrogen flow.

Deposition of rear contact. The 120 nm aluminum (Al) rear electrode of the solar cells was deposited on the glass substrates using resistive thermal evaporation, applying a current of 160 A under 10^{-6} mbar vacuum with a deposition rate of $0.3 \text{ nm}\cdot\text{s}^{-1}$. The Al film was coated with an aluminum zinc oxide (AZO) layer of 60 nm, deposited by radio frequency (RF) magnetron sputtering for 18 min with the conditions listed in Table S1 in SI.

Deposition of nc-Si:H layers. The samples were then transferred to an Electrorava plasma-enhanced chemical vapor deposition (PECVD) system where the silicon layers were deposited according to the n-i-p structure. A mixture of SiH_4 and H_2 defines the hydrogen dilution parameter ($\text{DH}(\%) = \text{H}_2 / (\text{H}_2 + \text{SiH}_4) \times 100$). In the case of the intrinsic silicon thin film a $\text{DH} = 97.3\%$ was used with a deposition pressure (P_{gas}) of 1 Torr and a power density (PW) equal to $139 \text{ mW}\cdot\text{cm}^{-2}$ at 75 MHz. The i-layer thickness deposited was $1.25 \mu\text{m}$. Adding trimethylboron (TMB, $\text{B}(\text{CH}_3)_3$) or PH_3 to the mixture of SiH_4 and H_2 produced p- or n-layers, respectively. A p-nc-Si:H layer of 25 nm was deposited with a $\text{DH} = 99.29\%$, $\text{RTMB} = \text{TMB} / (\text{H}_2 + \text{TMB} + \text{SiH}_4) = 0.56\%$, a $P_{\text{gas}} = 2.4$ Torr and a $\text{PW} = 90 \text{ mW}\cdot\text{cm}^{-2}$ at 13.56 MHz. As for the n-nc-Si:H layer, the parameters were: $\text{DH} = 96.7\%$, $\text{RPH}_3 = \text{PH}_3 / (\text{H}_2 + \text{PH}_3 + \text{SiH}_4) = 1\%$, $P_{\text{gas}} = 1$ Torr, $\text{PW} = 69 \text{ mW}\cdot\text{cm}^{-2}$ at 13.56 MHz and the obtained corresponding thickness was 50 nm.

Deposition of front contact and solar cell area delimitation. Transparent conductive oxide layers, made of 230 nm thick indium zinc oxide (IZO), were deposited by RF magnetron sputtering for 80 min over the nc-Si:H layers, with the conditions listed in Table S1.

To delimit solar cells of $3.5 \times 1.9 \text{ mm}$, the deposition of the IZO front electrode was carried out using a rectangular (PET) plastic mask with those dimensions. To assist in the external connection to the front TCO contact, an Al pad was deposited using another mask. Finally, an SF_6 plasma etching treatment was applied to remove the layer of nc-Si:H of the surrounding area, revealing the AZO–Al back contact. SF_6 was chosen as it does not affect the IZO layer in the dry etching process.

4.1.2 Parylene Deposition

Parylene-C [(C₁₆H₁₄Cl₂)_n] was deposited through vacuum chemical vapor deposition (CVD), using a PDS 2010 Labcoter 2 (Specialty Coating Systems). The final layer thickness was verified by profilometer.

4.1.3 Colloidal-Lithography

The surface patterning was performed through the use of a colloidal-lithography (CL) method involving three steps. The first step consisted in the deposition of a self-assembled monolayer of 1.6 μm polystyrene (PS) spherical colloids on the parylene surface through the Langmuir-Blodgett technique^[57] employing a *KSV NIMA* Langmuir-Blodgett deposition trough. We used 200 μL of dispersed PS microspheres purchased from *Microparticles GmbH* diluted in 600 μL of ethanol, maintaining a 25 μg/mL concentration.^[17] The surface tension threshold value was set to 18 mN/m and the substrate's pull speed was 2 mm/min. Subsequently, the parylene surface was patterned via reactive ion etching (RIE), in a *Trion Minilock Phantom III*, where the spheres served as physical etching mask. The RIE conditions are presented in Table 1. In this stage, two approaches were evaluated. The first consisted of RIE for up to 80 min with SF₆ and the second was performed for up to 10 min 48 s with O₂ (to activate and increase the surface roughness) followed by a fixed 1 min SF₆ RIE (to provide hydrophobicity). This process resulted in the formation of tapered cone microstructures on the parylene surface. The last step is the removal of the PS spheres with IPA and deionized water. The patterned structures were observed using a *Zeiss Auriga CrossBeam Workstation* scanning electron microscope (SEM).

Table 1 – Reactive ion etching (RIE) experimental parameters.

<i>Gas</i>	<i>Gas flow (sccm)</i>	<i>Pressure (mTorr)</i>	<i>Power (W)</i>
O ₂	50	45	50
SF ₆	50	45	50

4.1.4 Surface Characterization

Surface morphology analysis was performed using a *Zeiss Auriga CrossBeam Workstation* SEM and a *Hitachi TM 3030Plus Tabletop* SEM. Surface chemical composition was acquired via x-ray photoelectron spectroscopy, XPS (*Kratos Axis Supra*).

4.1.5 Contact Angle

Both static and dynamic water contact angle (CA) measurements were performed with a *DataPhysics OCA 15 Plus*, using 2 μL droplets of deionized water. The side view of the droplet was acquired by the system and the CA analysis was subsequently performed using the Laplace-Young approximation model.

4.1.6 Optical Characterization

The optical measurements were performed with a UV-VIS-NIR scanning spectrophotometer (*PERKIN ELMER lambda 950*), using a 15 cm diameter integrating sphere to obtain the total reflectance (R_T) spectra of the solar cells from 300 to 1100 nm. Total absorbance spectra were estimated by using the general formula: $A_T=1-R_T$.

4.1.7 Solar Cell Characterization

The photovoltaic response of the test solar cells was evaluated by measuring the current-voltage (I–V) curves with a LED Sun Simulator (*Oriel Vera Sol LSH-7520*) composed of 19 LEDs at individual wavelengths spaced over the relevant spectrum from 400 to 1100 nm, supplying a 1-sun illumination certified AAA in a 51x51 mm area. The external quantum efficiency (EQE) measurements were performed using a *Newport QuantX-300* system, equipped with a xenon lamp of 100 W, with a nominal illumination spot size of 0.8x1.1 mm.

5 Supporting Information

Supporting Information is available.

6 Acknowledgements

This work was financed by FEDER funds through the COMPETE 2020 Programme and National Funds through FCT (Portuguese Foundation for Science and Technology) under the projects UID/CTM/50025/2019, SuperSolar (PTDC/NAN-OPT/28430/2017), TACIT (PTDC/NAN-OPT/28837/2017) and LocalEnergy (PTDC/EAM-PEC/29905/2017). M. Alexandre also acknowledges the support from FCT through the PhD scholarship SFRH/BD/148078/2019.

7 References

- [1] M. Simon, E. L. Meyer, *Sol. Energy Mater. Sol. Cells* **2010**, *94*, 106.
- [2] A. Syafiq, A. K. Pandey, N. N. Adzman, N. A. Rahim, *Sol. Energy* **2018**, *162*, 597.
- [3] R. Karmouch, H. EL Hor, *J. Fundam. Renew. Energy Appl.* **2017**, *07*, 1.
- [4] A. Massi Pavan, A. Mellit, D. De Pieri, *Sol. Energy* **2011**, *85*, 1128.
- [5] N. N. Nipu, A. Saha, M. F. Khan, *Int. J. Eng. Technol.* **2016**, *6*, 9.
- [6] M. Mazumder, M. Horenstein, J. Stark, D. Erickson, A. Sayyah, S. Jung, F. Hao, in *ASME 2013 7th Int. Conf. Energy Sustain.*, American Society Of Mechanical Engineers, **2013**.
- [7] S. K. Sethi, G. Manik, *Polym. Plast. Technol. Eng.* **2018**, *57*, 1932.
- [8] X. Bi, B. P. Crum, W. Li, *J. Microelectromechanical Syst.* **2014**, *23*, 628.
- [9] X. Gao, X. Yan, X. Yao, L. Xu, K. Zhang, J. Zhang, B. Yang, L. Jiang, *Adv. Mater.* **2007**, *19*, 2213.
- [10] J. A. Howarter, J. P. Youngblood, *Adv. Mater.* **2007**, *19*, 3838.
- [11] W. Barthlott, C. Neinhuis, *Planta* **1997**, *202*, 1.
- [12] P.-G. de Gennes, F. Brochard-Wyart, D. Quéré, *Capillarity and Wetting Phenomena*, Springer New York, New York, NY, **2004**.
- [13] M. M. Tavakoli, K.-H. Tsui, Q. Zhang, J. He, Y. Yao, D. Li, Z. Fan, *ACS Nano* **2015**, *9*, 10287.
- [14] J. Y. Chen, W.-L. Chang, C. K. Huang, K. W. Sun, *Opt. Express* **2011**, *19*, 14411.
- [15] W. Qarony, M. I. Hossain, R. Dewan, S. Fischer, V. B. Meyer-Rochow, A. Salleo, D. Knipp, Y. H. Tsang, *Adv. Theory Simulations* **2018**, *1*, 1800030.
- [16] M. J. Mendes, A. Araújo, A. Vicente, H. Águas, I. Ferreira, E. Fortunato, R. Martins, *Nano Energy* **2016**, *26*, 286.
- [17] O. Sanchez-Sobrado, M. J. Mendes, S. Haque, T. Mateus, A. Araujo, H. Aguas, E. Fortunato, R. Martins, *J. Mater. Chem. C* **2017**, *5*, 6852.
- [18] X. H. Li, P. C. Li, D. Z. Hu, D. M. Schaadt, E. T. Yu, *J. Appl. Phys.* **2013**, *114*, 044310.
- [19] M. L. Brongersma, Y. Cui, S. Fan, *Nat. Mater.* **2014**, *13*, 451.
- [20] O. Sanchez-Sobrado, M. J. Mendes, S. Haque, T. Mateus, H. Aguas, E. Fortunato, R. Martins, *J. Mater. Chem. C* **2019**, *7*, 6456.
- [21] Y.-F. Huang, S. Chattopadhyay, Y.-J. Jen, C.-Y. Peng, T.-A. Liu, Y.-K. Hsu, C.-L. Pan, H.-C. Lo, C.-H. Hsu, Y.-H.

- Chang, C.-S. Lee, K.-H. Chen, L.-C. Chen, *Nat. Nanotechnol.* **2007**, *2*, 770.
- [22] C. Ulbrich, C. Zahren, J. Noll, A. Gerber, K. Hermans, A. Lambertz, U. Rau, in *Proc. 26th Eur. Photovolt. Sol. Energy Conf. Exhib.*, **2011**, pp. 2329–2335.
- [23] O. Sanchez-Sobrado, M. J. Mendes, T. Mateus, J. Costa, D. Nunes, H. Aguas, E. Fortunato, R. Martins, *Sol. Energy* **2020**, *196*, 92.
- [24] E. Meng, P.-Y. Li, Y.-C. Tai, *J. Micromechanics Microengineering* **2008**, *18*, 045004.
- [25] H. Kim, J. Lee, B. Kim, H. R. Byun, S. H. Kim, H. M. Oh, S. Baik, M. S. Jeong, *Sci. Rep.* **2019**, *9*, 15461.
- [26] H. Kim, H. R. Byun, B. Kim, S. H. Kim, H. M. Oh, M. S. Jeong, *J. Korean Phys. Soc.* **2018**, *73*, 1675.
- [27] A. Kiazadeh, H. L. Gomes, P. Barquinha, J. Martins, A. Rovisco, J. V. Pinto, R. Martins, E. Fortunato, *Appl. Phys. Lett.* **2016**, *109*, 1.
- [28] M. Golda-Cepa, K. Engvall, M. Hakkarainen, A. Kotarba, *Prog. Org. Coatings* **2020**, *140*, 105493.
- [29] L. Zhang, Y. Liu, Z. Li, W. Wang, *Micromachines* **2018**, *9*, 162.
- [30] J. Ortigoza-Diaz, K. Scholten, C. Larson, A. Cobo, T. Hudson, J. Yoo, A. Baldwin, A. Weltman Hirschberg, E. Meng, *Micromachines* **2018**, *9*, 422.
- [31] M. Gołda, M. Brzychczy-Włoch, M. Faryna, K. Engvall, A. Kotarba, *Mater. Sci. Eng. C* **2013**, *33*, 4221.
- [32] T. Trantidou, T. Prodromakis, C. Toumazou, *Appl. Surf. Sci.* **2012**, *261*, 43.
- [33] V. Satulu, M. Ionita, S. Vizireanu, B. Mitu, G. Dinescu, *Molecules* **2016**, *21*, 1711.
- [34] L. Schneider, M. Laustsen, N. Mandsberg, R. Taboryski, *Sci. Rep.* **2016**, *6*, 21400.
- [35] R. N. Wenzel, *Ind. Eng. Chem.* **1936**, *28*, 988.
- [36] A. B. D. Cassie, S. Baxter, *Trans. Faraday Soc.* **1944**, *40*, 546.
- [37] B. Bhushan, M. Nosonovsky, *Philos. Trans. R. Soc. A Math. Phys. Eng. Sci.* **2010**, *368*, 4713.
- [38] S. Wang, L. Jiang, *Adv. Mater.* **2007**, *19*, 3423.
- [39] K. Liu, X. Yao, L. Jiang, *Chem. Soc. Rev.* **2010**, *39*, 3240.
- [40] T. Verho, J. T. Korhonen, L. Sainiemi, V. Jokinen, C. Bower, K. Franze, S. Franssila, P. Andrew, O. Ikkala, R. H. A. Ras, *Proc. Natl. Acad. Sci.* **2012**, *109*, 10210.
- [41] M. Resnik, R. Zaplotnik, M. Mozetic, A. Vesel, *Materials (Basel)*. **2018**, *11*, 311.
- [42] J. F. Moulder, W. F. Stickle, P. E. Sobol, K. D. Bomben, *Handbook of X-Ray Photoelectron Spectroscopy*, Physical Electronics, Inc., Eden Prairie, Minnesota, **1995**.
- [43] F. Walther, P. Davydovskaya, S. Zürcher, M. Kaiser, H. Herberg, A. M. Gigler, R. W. Stark, *J. Micromechanics Microengineering* **2007**, *17*, 524.

- [44] K. S. Kim, K. H. Lee, K. Cho, C. E. Park, *J. Memb. Sci.* **2002**, *199*, 135.
- [45] J. Chai, F. Lu, B. Li, D. Y. Kwok, *Langmuir* **2004**, *20*, 10919.
- [46] T. Koishi, K. Yasuoka, S. Fujikawa, T. Ebisuzaki, X. C. Zeng, *Proc. Natl. Acad. Sci.* **2009**, *106*, 8435.
- [47] D. Murakami, H. Jinnai, A. Takahara, *Langmuir* **2014**, *30*, 2061.
- [48] N. A. Patankar, *Langmuir* **2004**, *20*, 7097.
- [49] N. Gao, Y. Yan, *J. Bionic Eng.* **2009**, *6*, 335.
- [50] N. Coron, C. Cuesta, E. García, C. Ginestra, T. A. Girard, P. de Marcillac, M. Martínez, Y. Ortigoza, A. Ortiz de Solórzano, C. Pobes, J. Puimedón, T. Redon, M. L. Sarsa, L. Torres, P. Valko, J. Á. Villar, *EPJ Web Conf.* **2014**, *65*, 02001.
- [51] M. Sasani Ghamsari, S. Alamdari, W. Han, H.-H. Park, *Int. J. Nanomedicine* **2016**, *12*, 207.
- [52] S. Manzoor, Z. J. Yu, A. Ali, W. Ali, Z. C. Holman, in *2017 IEEE 44th Photovolt. Spec. Conf.*, IEEE, **2017**, pp. 1228–1232.
- [53] M. J. Mendes, S. Haque, O. Sanchez-Sobrado, A. Araújo, H. Águas, E. Fortunato, R. Martins, *iScience* **2018**, *3*, 238.
- [54] “Lumerical Inc.,” can be found under <https://www.lumerical.com/products/>, **n.d.**
- [55] S. Haque, M. J. Mendes, O. Sanchez-Sobrado, H. Águas, E. Fortunato, R. Martins, *Nano Energy* **2019**, *59*, 91.
- [56] M. Alexandre, M. Chapa, S. Haque, M. J. Mendes, H. Águas, E. Fortunato, R. Martins, *ACS Appl. Energy Mater.* **2019**, *2*, 2930.
- [57] A. Emoto, E. Uchida, T. Fukuda, *Colloids Surfaces A Physicochem. Eng. Asp.* **2012**, *396*, 189.